Research Article

Israel Journal of Chemistry

doi.org/10.1002/ijch.202100079

The Impact of Chiral Citronellyl-Functionalization on Indolenine and Anilino Squaraine Thin Films

Frank Balzer,[a] Marvin F. Schumacher,[b] Sara Mattiello,[c] Matthias Schulz,[b] Jennifer Zablocki,[b] Marc Schmidtmann,[d] Klaus Meerholz,[e] N. Serdar Sariciftci,[f] Luca Beverina,[c] Arne Lützen,[b] and Manuela Schiek*[f, g, h]

Dedicated to Prof. N.S. Sariciftci on the occasion of his 60th birthday.

Abstract: The impact on chiral aggregation in solution processed and thermally annealed thin films of two indolenine and one anilino squaraines with chiral (*S*)-citronellyl functionalization at the nitrogen of the squaraine backbone is investigated. A pseudo polymorphic crystal structure is obtained for one of the indolenine squaraines, but thin films of both compounds are basically non-aggregated and truly isotropic as evidenced by spectroscopic ellipsometry. The anilino squaraine coalesces and readily aggregates to circular dichroic but discontinuous thin films. The extent of circular dichroism correlates with the morphology of the samples, which is quantified by Mueller matrix polarimetry in combination with atomic force microscopy. The shape of the CD spectra reinforces the hybrid Frenkel and charge-transfer excitonic nature of the characteristic double hump signatures within unpolarized absorbance spectra of previously investigated non-chiral anilino squaraines with linear alkyl chain functionalization. Such excitonic CD offers an additional design parameter for next-generation opto-electronic devices.

Keywords: squaraine · circular dichroism · micro-morphology · charge-transfer excitons

1. Introduction

Squaraine dyes are attractive due to their intense interactions with visible to near-infrared light combined with environmental robustness and friendliness as well as convenient chemical accessibility.[1–4] This results in a wide-spread application potential covering photovoltaics, photocatalysis, biomedicine and sensing devices.[5–11] Squaraines (SQs) can adopt different structural motifs such as anilino or indolenine type SQs, Figure 1. Both types are donor-acceptor-donor small molecular compounds with zwitterionic resonant structures causing pronounced *intra*molecular charge-transfer states. These in turn give rise to strong *inter*molecular excitonic interactions[12] that can be of Coulombic nature (Frenkel excitons)[13] or involve *inter*molecular charge-transfer (ICT) excitons.[14] This is basically depending on molecular packing geometry steered by terminal *N* or acceptor-core substitution in case of indolenine SQs.[15]

Acceptor-core substitution changes the molecular symmetry and installs a permanent dipole moment to the otherwise

[a] *F. Balzer*
SDU Centre for Photonics Engineering, Mads Clausen Institute, University of Southern Denmark,
Alsion 2, DK-6400 Sønderborg, Denmark
[b] *M. F. Schumacher, M. Schulz, J. Zablocki, A. Lützen*
Kekulé-Institute for Organic Chemistry and Biochemistry, University of Bonn,
Gerhard-Domagk-Str. 1, D-53121 Bonn, Germany
[c] *S. Mattiello, L. Beverina*
Department of Materials Chemistry and INSTM, University of Milano-Bicocca,
Via R. Cozzi 53, I-20125 Milano, Italy
[d] *M. Schmidtmann*
Department of Chemistry, University of Oldenburg,
Carl-von-Ossietzky-Str. 9–11, D-26129 Oldenburg, Germany
[e] *K. Meerholz*
Physical Chemistry, University of Cologne,
Greinstr. 4–6, D-50939 Cologne, Germany
[f] *N. Serdar Sariciftci, M. Schiek*
Linz Institute for Solar Cells, Johannes Kepler University,
Altenberger Str. 69, A-4040 Linz, Austria
E-mail: manuela.schiek@jku.at
[g] *M. Schiek*
Center for Surface- and Nanoanalytics and Linz Institute for Solar Cells,
Johannes Kepler University,
Altenberger Str. 69, A-4040 Linz, Austria
[h] *M. Schiek*
Institute of Physics, University of Oldenburg,
Carl-von-Ossietzky-Str. 9–11, D-26129 Oldenburg, Germany

Supporting information for this article is available on the WWW under https://doi.org/10.1002/ijch.202100079

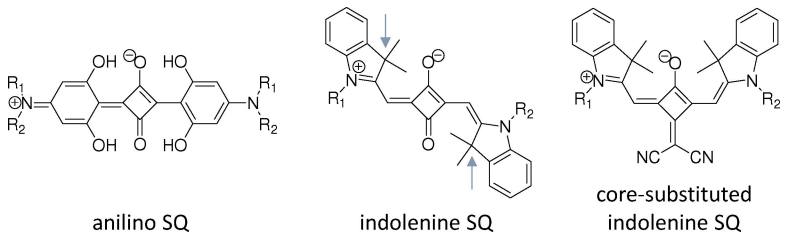

Figure 1. Structural motifs of squaraines (SQs): anilino SQ, indolenine SQ and acceptor-core substituted indolenine SQ. Terminal *N* substitutions ($R_1 \neq R_2$ or $R_1 = R_2$) are typically linear, branched or cyclic alkyl rests, that can also be chiral. The arrows indicate further optional positions for structural variations of indolenine SQs.

quadrupolar SQs.[16] This core-substitution was found to be beneficial for photovoltaic performance[17] since it inhibits photophysical dark-states[18] and fosters packing leading to ICT interactions.[19,20] Further variations of the indolenine SQ motif are replacing the carbon at the indicated ring position in Figure 1 with a sulfur or selenium atom to increase charge mobility for transistor applications.[21] Anilino SQs are basically modified by terminal *N* substitution. In case of bulky rests Coulombic interactions prevail and the optical spectra are shaped by a Davydov splitting.[13] Linear alkyl chains allow close slip-stack packing and ICT interactions that result in marked spectral double hump signatures, which are interpreted as mixed states of a Coulombic H-aggregate and a charge separated state.[22]

Chiral substitution adds another molecular design parameter to implement excitonic circular dichroism (CD), which is the differential absorption of circular polarized light of opposite handedness. The chiroptical response is mediated by the chiral supramolecular arrangement of the molecular backbones carrying the optical transition dipole moment, i.e. by the excitonic coupling of the molecules.[23–25] The chiral groups typically act as steering agent for the packing, but not directly cause the chiroptical response. For indolenine SQs there has also been an approach to integrate the chiral center into the backbone at the indicated position in Figure 1.[26] Terminal chiral functionalization, such as cyclic pyrrol-[27] and prolinol-derived[28] groups, has proven feasibility for anilino squaraines to induce an excitonic circular dichroic response in aggregated thin film samples. Actually, the prolinol moiety successfully generated a largely enhanced CD response, more than a factor of 100 larger than generic chiral organic thin films, solely based on the nature of the excitonic coupling. Yet, the critical role of ICT for the enhancement is under debate.[29] However, such a strong excitonic CD effect has proven to be functional in circular polarized light detectors without the need for further external polarization manipulating elements.[30]

Selective sensitivity to – and emissivity of – circular polarized light is a central theme for the development of advanced photonic and optoelectronic devices as well as novel spectroscopic and imaging tools. Rational design of molecular materials is a key to success.[31,32] A strategy that avoids costly separation of racemic mixtures is to start with abundant chiral pool reactants such as terpenes and in particular citronellol. Citronellyl (3,7-dimethyloctyl) substituents are widely used in racemic form to enhance solubility of a compound.[15,33–36] Basically the *S*-enantiomeric form was shown to efficiently imprint supramolecular chirality to graphitic nanotubes,[37] perylene bisimides,[38] and poly-thiophenes[39,40] as well as poly-fluorenes.[41–45]

In this work, we study the impact on chiral aggregation in solution processed and thermally annealed thin films of two indolenine and one anilino SQs with chiral (*S*)-citronellyl *N* terminal functionalization. Even though we could resolve a crystal structure for one of indolenine SQs, crystallization in thin films was barely obtained due to volatility of the material. For the anilino SQ we could quantify its circular dichroic response in thin films, which was strongly affected by the morphology of the samples. However, the shape of the CD spectra is significant and reinforces the interpretation of the characteristic double hump signatures of unpolarized absorbance spectra of previously investigated non-chiral anilino squaraines with linear alkyl chain functionalization.[14,22]

2. Mono- and Bis-Citronellyl Functionalized Indolenine Squaraines mCi-SQ and bCi-SQ

The synthesis of the two indolenine compounds (***S***)-**mCi-SQ** and (***S,S***)-**bCi-SQ**, carrying one or two (*S*)-citronellyl chiral groups at the indolenic nitrogen, respectively, has been facilitated following the scheme presented in Figure 2.

Directly from the purification procedure, single crystals of **bCi-SQ** suitable for X-ray analysis have been obtained. Unfortunately, this was a pseudo-polymorph structure including four *n*-hexane solvent molecules together with four **bCi-SQ** molecules within the body-centered monoclinic unit cells with a chiral *I*2 space group. Details on the unit cell parameters can be found in Table 1. The structure can be seen in Figure 3 omitting the solvent molecules for clarity of presentation. The molecules organize in two columnar π stacks tilted with respect to each other, with an inclination angle of 20° with respect to the crystallographic *c*-axis in the projection viewing along the *a*-axis, Figure 3(a). Along the *b*-axis, the molecules are arranged side-by-side, no staircase-shape, Figure 3(b). In (c) and (d) views slightly offset from the

Israel Journal of Chemistry

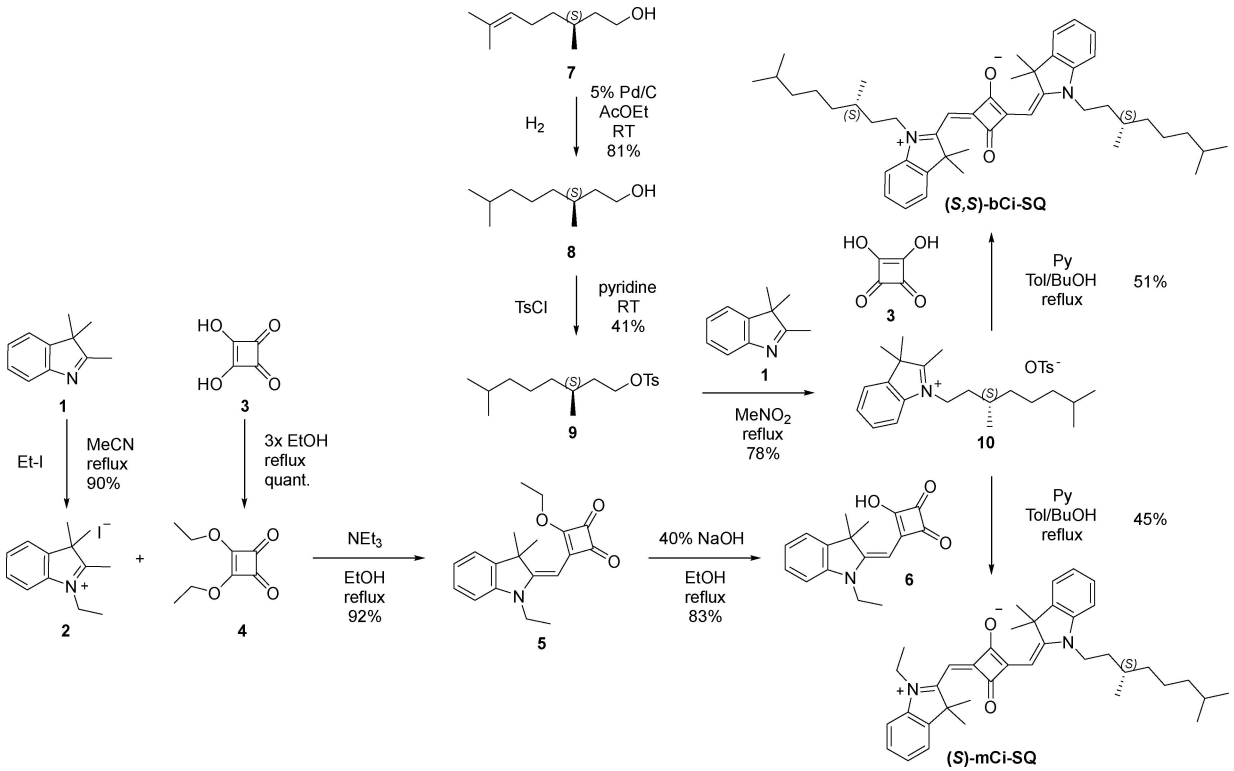

Figure 2. Schematic synthesis protocol for the two indolenine compounds **(*S*)-mCi-SQ** (or shortly **mCi-SQ**) and **(*S,S*)-bCi-SQ** (or shortly **bCi-SQ**). For this, 1-ethyl-2,3,3-trimethyl-3H-indoliumiodide **2**,[46] 3,4-diethoxycyclobut-3-ene-1,2-dione **4**,[46] 3-ethoxy-4-((1-ethyl-3,3-dimethylindolin-2-ylidene)methyl)cyclobut-3-ene-1,2-dione **5**[46,47] and 3-((1-ethyl-3,3-dimethyl-indolin-2-ylidene)methyl)-4-hydroxy-cyclobut-3-ene-1,2-dione **6**[46,47] were synthesized according to the cited references. The other syntheses were done by modified versions of previously reported protocols in the literature as indicated in the experimental section.

Table 1. Unit cell parameters of **(*S,S*)-bCi-SQ** (CCDC 2094899).

space group	*a* (Å)	*b* (Å)	*c* (Å)	*α* (°)	*β* (°)	*γ* (°)	*Z*
*I*2 (5)	19.0769(7)	9.3541(4)	27.3099(13)	90	108.953(2)	90	4

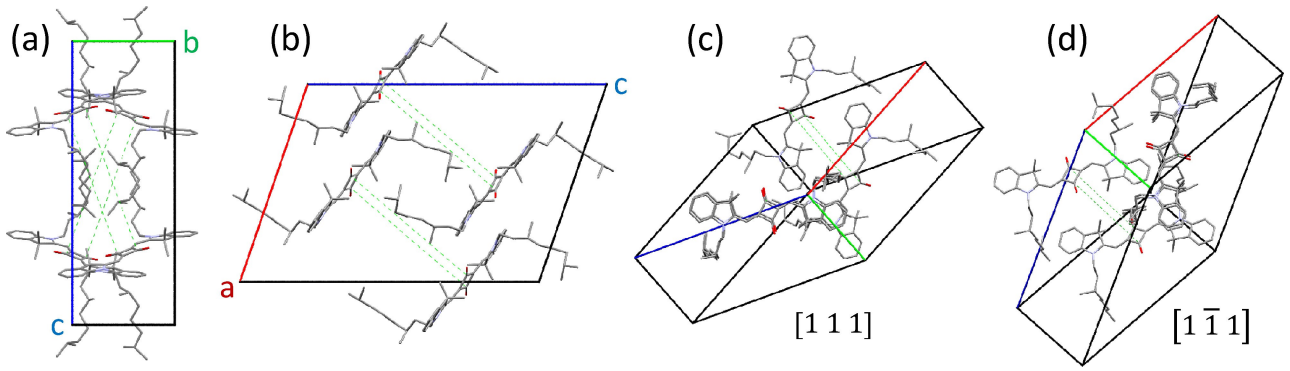

Figure 3. Visualization of the monoclinic pseudo crystal structure with space group *I*2 of **bCi-SQ** (CCDC code 2094899) omitting the *n*-hexane solvent molecules. (a) View along the *a*-axis, (b) view along the *b*-axis. (c) and (d) are views along the two molecular stacking directions [*u v w*] = [1 1 1] and [1 $\bar{1}$ 1], respectively, with a slight offset to show the stacking molecules. Green dashed lines are added to indicate the stacking squaraic central cores. The angle between the stacking directions is 40° in the projection viewing along the crystallographic a-axis in (a). The *c*-axis is the angle bisector.

perspective along the columnar stack axis pointing in [*u v w*] = [1 1 1] and [1 $\bar{1}$ 1] directions, respectively, are presented.

Despite the readiness to crystallize in the bulk, spincasted thin films were perfectly isotropic for both indolenine SQs. The layers are also reasonably smooth and continuous, see atomic force microscopy images in the Supporting Information Figure S1. The normalized absorbance spectra and the complex refractive index of **mCi-SQ** and **bCi-SQ** without thermal post-treatment are shown in Figure 4. The absorbance peaks at the same spectral position 675 nm with a vibronic shoulder at 615 nm for both compounds as shown in Figure 4(a). The energetic difference is roughly 180 meV, which is typical for C=C stretching and ring breathing vibrations of conjugated organic molecules.[12] The vibronic progression is slightly more pronounced for the **mCi-SQ**, relative peak height 0.62 versus 0.56 for **bCi-SQ**. This results already in a slightly different color impression of the thin films as illustrated by the insets showing photographs of the samples on a white background. Consequently, the isotropic complex refractive index is very similar for the indolenine compounds, Figure 4(b). The extinction coefficients *k* are remarkably large being on the order of 1.6 to 1.7 at maximum for **mCi-SQ** and **bCi-SQ**, respectively. This is among the highest values of

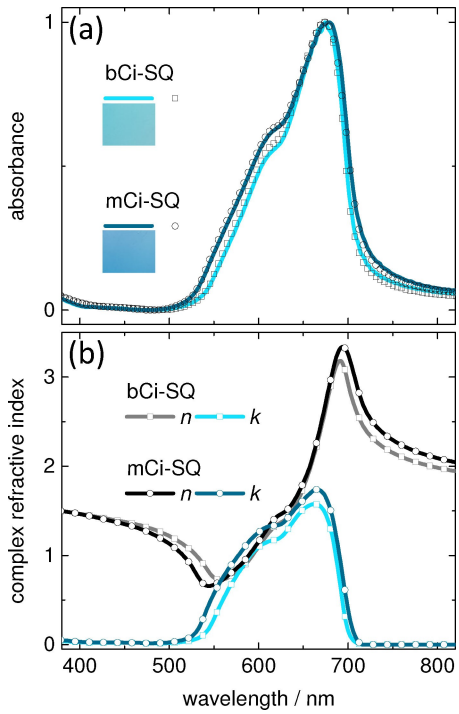

Figure 4. (a) Normalized absorbance of **bCi-SQ** (squares) and **mCi-SQ** (circles) spincasted thin films without thermal post-treatment. Solid lines are measured spectra and symbols show fit data obtained from the simultaneous fitting of ellipsometric and transmission intensity data. Insets display photos of samples on white background. (b) Isotropic real refractive index *n* and extinction coefficient *k* of **bCi-SQ** (squares) and **mCi-SQ** (circles) obtained by spectroscopic ellipsometry.

conjugated polymers typically used for highly efficient solar cells,[48] but yet is exceeded by crystalline anilino squaraine thin films.[49] Since no distinct molecular aggregation could be evidenced for the isotropic **mCi-SQ** and **bCi-SQ** it is self-explaining that neither excitonic CD signals, which would arise from chiral molecular aggregation or crystallization, could be detected. This is in line with a study, that compares chiral functionalization at the backbone of indolenine SQ with chiral terminal substitution.[26] This study utilized an acceptor-core substituted indolenine and covered only colloidal aggregation in solution, however, the chiral (*S*)-citronellyl at the nitrogen atom showed inferior (chiral) aggregation behavior.

Subsequent thermal annealing of thin films after solution processing is a common strategy to induce aggregation and even crystallization, but not for the present compounds **mCi-SQ** and **bCi-SQ**. They remained isotropic for annealing temperatures up to 90 °C, and for slightly higher temperatures then suddenly coalesced and evaporated off the substrate. In case of **bCi-SQ** we could capture a sample, which was covered with residual crystalline material by timed removal from the hotplate before all material was sublimed. The result can be seen in Figure 5(a), which shows the amoeba-like shape remains of **bCi-SQ** on the substrate. The yellow rectangle and the yellow square mark the areas, that have been imaged by intermittent contact mode AFM and displayed in (b) and (c), respectively. Cross-polarized microscopy imaging, Figure 5(d), revealed birefringence, and thus, crystallinity of the remaining **bCi-SQ**. The AFM measured the edges to be taller than the core area, which finds its expression in different interference colors: greenish for the taller rim and brownish for the core area. There were also shallow droplet-like features imaged by AFM in (b) that certainly were amorphous and consequently are invisible between crossed polarizers.

In the next step, a sufficiently homogeneous core area was selected as marked by the white circle in Figure 5(d) for spatially and polarization resolved spectroscopy. In (e) linear polarized absorbance spectra for a full rotation of the linear polarizer are shown as two-dimensional contour plot. Two absorption maxima at 576 nm and at 693 nm became visible that peak alternately at 90° and repeat themselves every 180°. Figure 5(f) shares the wavelength scale with (e) and displays the absorbance spectra in one dimensional representation for a 90° rotation of the linear polarizer. Starting and ending points were at a position where the short and long wavelength peaks were at maximum, respectively. Such spectral polarization course is typical for a Davydov splitting arising from molecular aggregates with at minimum two translationally invariant molecules per primitive unit cell interacting.[12] The short wavelength peak is the upper (UDC) and the long wavelength peak the lower Davydov component (LDC). The Davydov splitting amounts to 0.36 eV which is large, indicative for strong intermolecular interactions, but yet typical for squaraine compounds.[13,15,49]

The overall coverage with **bCi-SQ** material of the above discussed sample was very low, therefore the sample appeared

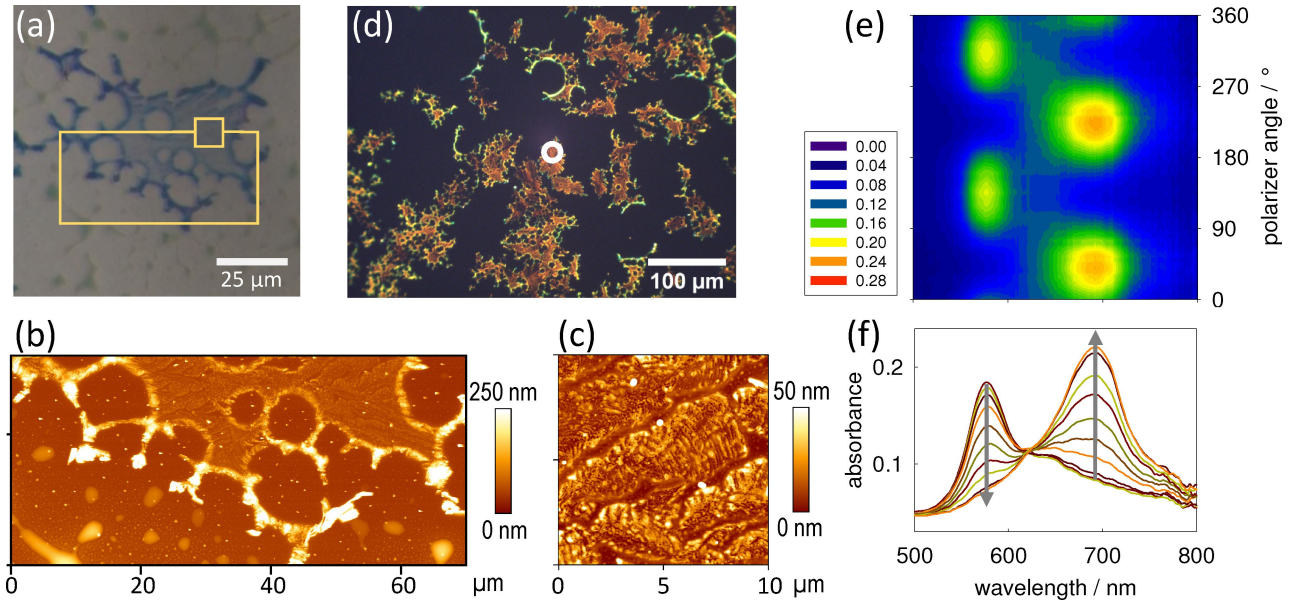

Figure 5. (a) Unpolarized brightfield microscopy image of a textured and discontinuous, micro-crystalline **bCi-SQ** sample. The yellow rectangle and the yellow square mark the areas imaged by AFM in (b) and (c), respectively. The edges of the amoeba-like shape **bCi-SQ** structure were taller and appeared greenish in cross-polarized microscopy imaging (d) while the core areas were flatter and seemed brownish. Shallow droplet-like amorphous aggregates were dark between crossed polarizers. The white circle in (d) indicates the core area, where polarized transmission spectra have been recorded. These spectra are shown as absorbance ($=-\log(T)$) in the two-dimensional contour plot (e) for a full rotation of the linear polarizer. Horizontal axis: wavelength in nanometers (same scale as in (f)), vertical axis = polarizer angle in degrees. (f) displays the absorbance spectra versus wavelength for 90° rotation of the linear polarizer starting at maximum UDC and ending at maximum LDC. The arrows guide the eye to illustrate the evolution of peaks.

silent in thin film XRD analysis. But we could generate by dropcasting and thermal annealing a thick, crystalline **bCi-SQ** sample, which returned a signal in thin film XRD analysis, Figure S2 in the Supporting Information. For optical spectroscopy in transmission, such dropcasted samples were too thick. The single diffraction peak obtained by XRD is characteristic for a single crystallographic plane being parallel to the substrate. However, this signal does not match at all with the calculated powder pattern of the **bCi-SQ** pseudo-polymorph found for bulk crystals. Thus, the **bCi-SQ** adopts a different crystal polymorph in processed thin films.

3. *n*-Octyl Citronellyl Functionalized Anilino Squaraine nOCi-SQ

The synthesis scheme for the anilino SQ compound (***S,S***)-**nOCi-SQ** can be seen in Figure 6 following adopted, previously reported protocols.[2]

Even for spincasted **nOCi-SQ** samples without thermal treatment a certain molecular aggregation and preferential orientation became evident by optical spectroscopy. A normalized absorbance spectrum can be seen in Figure 7(a) displaying two spectral signatures peaking at 564 nm and 663 nm. Fitting of ellipsometric data required an anisotropic uniaxial model giving two data sets for the complex refractive index: ordinary, n_o and k_o, within the plane, and extra-ordinary, n_e and k_e, perpendicular to the plane of the thin film, Figure 7(b). This means that the organization of molecules or aggregates is random within the plane of the thin film, at least on a dimensional scale that is smaller than the wavelength of the probing light. The samples showed no linear dichroism or birefringence on a macroscopic or microscopic scale under typical normal incidence optical inspection. But there is a certain preferred orientation of molecules and aggregates parallel to the surface. For other aggregated micro-crystalline anilino squaraine thin films it was found, that the molecular stacking direction lies within the plane of the thin film,[13,14,27] which is also a likely case for the present **nOCi-SQ** samples. The fitted uniaxial complex refractive index serves well to calculate the absorbance spectra. In Figure 4(a) the solid line shows a measured absorbance spectrum together with a fitted spectrum (squares) from the ellipsometric data analysis procedure.

This was different for spincasted **nOCi-SQ** thin films with subsequent annealing, here at 100 °C. The absorbance spectra for as cast and annealed samples basically looked the same, only a slight blue-shift of the short wavelength peak to 557 nm was noticeable. The solid lines in Figure 7(c) show measured absorbance spectra for variable layer thicknesses of annealed samples. But the uniaxal complex refractive index determined for such samples, Figure 7(d) reproduces the measured absorbance spectra rather poorly. The fitted absorbance spectra

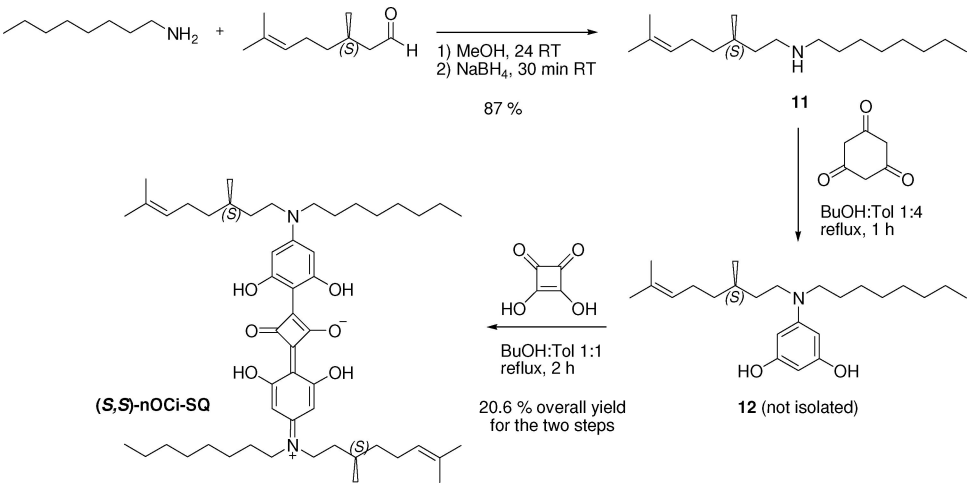

Figure 6. Schematic synthesis protocol for the anilino squaraine compound (***S,S***)**-nOCi-SQ** (shortly **nOCi-SQ**). Note that the (*S*)-citronellyl group has not been hydrated for this compound.

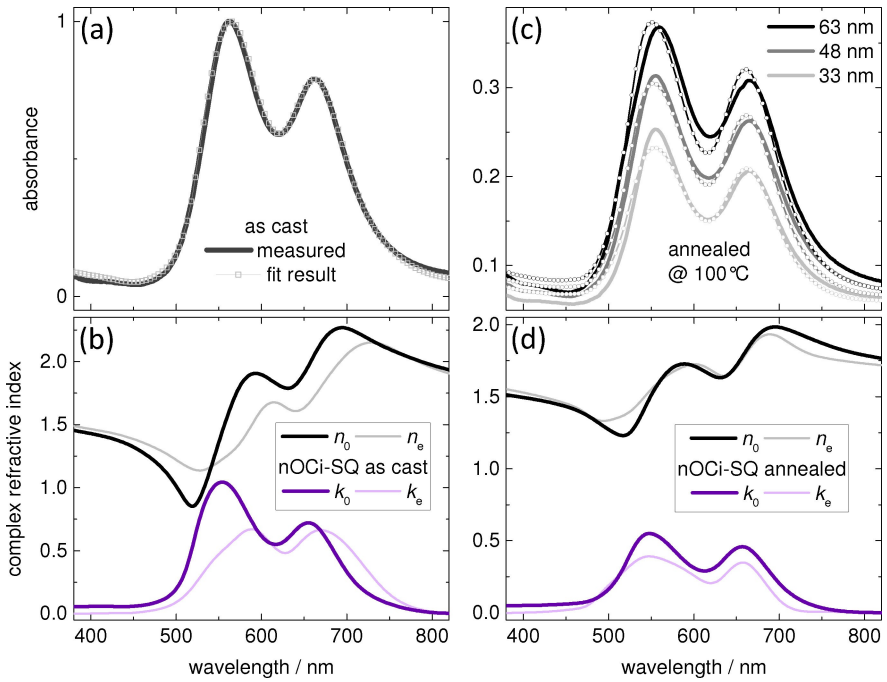

Figure 7. (a) Normalized absorbance of spincasted **nOCi-SQ** without thermal post-treatment. Solid line is the measured spectrum and symbols show fit data obtained from the simultaneous fitting of ellipsometric and transmission intensity data. (b) Uniaxial anisotropic complex refractive index of a **nOCi-SQ** thin film without annealing. Thick and thin lines denote the ordinary components n_o and k_o and the extra-ordinary components n_e and k_e, respectively. (c) Absorbance as measured (solid lines) of spincasted and subsequently annealed at 100 °C **nOCi-SQ** samples having three different coverages. Note that the thickness values indicated in the graph are nominal estimates as obtained from ellipsometric fitting. Symbols show fit data obtained from the simultaneous fitting of ellipsometric and transmission intensity data. (d) Averaged uniaxial anisotropic complex refractive index of spincasted **nOCi-SQ** samples annealed at 100 °C. Thick and thin lines denote the ordinary components n_o and k_o and the extra-ordinary components n_e and k_e, respectively.

from the ellipsometric data analysis procedure are shown as thin lines with circles in Figure 7(c). Three layer thicknesses and a non-normalized representation are chosen to illustrate that the deviation between measured and fitted absorbance spectra depends on sample parameters, here variable layer thickness. It is also conspicuous that the extinction coefficients for the annealed samples are significantly reduced (d) compared to the non-annealed samples (b). Since we conducted a combined fitting of multiple samples with six different thicknesses ranging roughly from 30 nm to 80 nm,

this means that there was no common uniaxial complex refractive index to describe all samples sufficiently. In other words, the complex refractive index of annealed **nOCi-SQ** samples varies with layer thickness. Thus, they describe no longer a material property but a sample property depending on processing parameters.

This is supported by inspection of the **nOCi-SQ** sample's morphology. Figure 8 displays intermittent contact mode atomic force microscopy (AFM) images of a sample without annealing in (a) and two samples annealed at 100 °C in (b) and (c). The as cast **nOCi-SQ** sample consisted of a continuous and smooth thin film with an average surface roughness *R*a just below 2 nm. Exact values are given in the caption of Figure 8. Upon thermal annealing, here 100 °C, microsized fibril-shaped aggregates emerged making the samples discontinuous. With this, it becomes problematic to define an accurate layer thickness. The values given for the annealed samples can be rather understood as nominal layer thicknesses or as indicator for a certain coverage with material. The fibril formation became more pronounced with increasing material coverage. Figures 8(b) and (c) show samples with 44 nm and 79 nm nominal thicknesses, respectively, and the average surface roughness *R*a increased from almost 9 nm to almost 12 nm. Such samples can only poorly be analyzed with standard spectroscopic ellipsometry. Therefore, the uniaxial complex refractive index given for the annealed **nOCi-SQ** samples in Figure 7(d) have only an estimative character.

Coming back to the absorbance spectra, the spectral shape is very much reminiscent of the characteristic double hump spectral signatures of *n*-alkyl anilino SQ thin films.[14] The physical origin of these peaks is mixing of a Coulombic Frenkel exciton with a charge separated state from ICT and redistribution of the shared oscillator strength.[22] The Frenkel exciton has the character of an H-aggregate, and the ICT is possible because of closely π-stacked molecular backbones as evidenced by the single crystal structures. Based on the primitive crystallographic unit cell containing only a single molecule, a Davydov splitting can be ruled out as reason for the double peaks.[12] For simplicity we name the two peaks the H-band (shorter wavelength) and the CT-band (longer wavelength). We assume that the (*S*)-citronellyl chain, even though it is not fully linear, does not disturb tight slip-stacked π-stacking of the **nOCi-SQ** backbones enabling ICT interactions. Therefore, we consider the hybrid Frenkel-ICT-exciton theory as valid also for the **nOCi-SQ**. However, the packing motif cannot be the same as in case of the *n*-alkyl anilino SQs,[14] which show fully parallel alignment of the backbones carrying the transition dipole moment. For the **nOCi-SQ** a chiral arrangement must be realized at least for the temperature treated samples since they show a pronounced circular dichroic response. Unfortunately, we cannot say more about the molecular packing here. All **nOCi-SQ** samples were silent in thin film XRD investigation, and no bulk single crystals could be obtained from the powder.

By Mueller matrix polarimetry[50,51] in normal incidence transmission we have analyzed the circular dichroism of the **nOCi-SQ** samples. Note that our instrumentation did not provide spatial resolution, and consequently we obtained only effective or averaged spectra in case of micro-structured samples. While the as cast samples were CD-silent, the thermally annealed samples showed a significant CD-response, Figure 9(a). The CD signal has been normalized to the unpolarized absorbance of the samples to give the dissymmetry factor *g*,[23–25] which is plotted for varying nominal layer thicknesses. The shape of the CD-spectra was the same for all sample coverages. The H-band showed a bisignate CD signal with a negative lobe at 515 nm and a positive lobe peaking at 575 nm. The zero-crossing of this bisignate signal is at the maximum peak position of the H-band of the unpolarized **nOCi-SQ** absorbance. According to exciton chirality rules, this hints to a right-handed helical organization of the molecular transition dipole moments and their Coulombic coupling.[12,23–25] The long wavelength CT-band gave another CD signal, which was monosignate, positive only and peaked slightly red-shifted compared to the unpolarized absorbance at 670 nm. The characteristic shape of the **nOCi-SQ** CD-spectrum reinforces the interpretation of the double hump spectral signatures of the unpolarized absorbance spectra as hybrid Frenkel and charge transfer exciton.[22] Furthermore, the humps reveal their original nature in the CD-spectrum: the

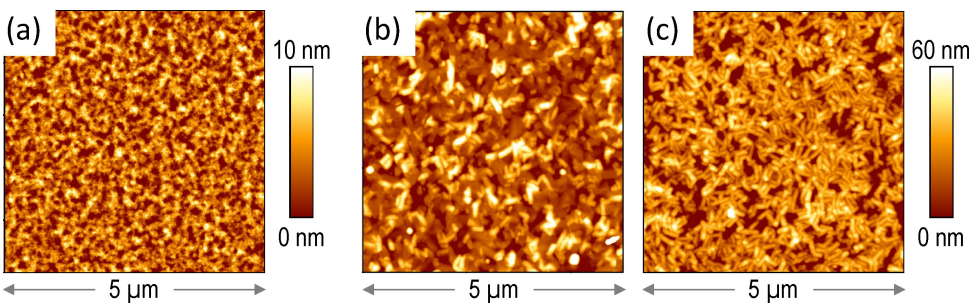

Figure 8. Intermittent contact mode AFM images of spincasted **nOCi-SQ** samples (a) without thermal treatment (layer thickness 32 nm, *R*a = 1.89(2) nm and *R*q = 2.37(2) nm) and thermally annealed at 100 °C with (b) 44 nm (*R*a = 8.7(2) nm, *R*q = 14.0(5) nm) and (c) 79 nm (*R*a = 11.8(2) nm and *R*q = 16.1(3) nm) nominal film thickness. Scan range is the same for all images being 5 µm × 5 µm, but height scale is six times smaller for the non-annealed sample in (a).

short wavelength band retains the bisignate shape originating from the Coulombic H-aggregate, while the long wavelength band returns a monosignate CD peak shape arising from the ICT. However, the impact of ICT on CD spectra is a largely underexplored topic, and deserves further theoretical analysis in the future.

Another striking aspect of the **nOCi-SQ** CD spectra is their dependence on nominal layer thickness. Figure 9(b) illustrate the evolution of the dissymmetry factor g of CD peak extrema with coverage. All three g peaks, both negative and positive lobe of the H-band, 515 nm and 575 nm, respectively, and the positive CT-band peak at 670 nm first increased in magnitude with layer thickness up to 60 nm and saturated for the largest nominal layer thickness close to 80 nm. The bisignate signal was asymmetric with a more pronounced negative lobe than positive lobe. For the highest value, the negative lobe resulted in a value of more than 0.2 for $|g|$, which was twice as much as the corresponding positive lobe maximum at around 0.1. The CT-band maximum was lagging behind with approximately 0.07 for the larger coverages. Actually, the g value better correlated with surface roughness of the samples, Figure 9(c), rather than with the nominal layer thickness. Note that even though the thickness values need to be considered with care, the g value solely depends on measured data, that is CD (ΔAbs^{CP}) and absorbance ($Abs = -\log(T)$) spectra: $g = \frac{\Delta Abs^{CP}}{Abs}$. However, CD spectra normalized to the nominal film thickness showed the same trend in coverage dependence, see Supporting Information Figure S3.

Nevertheless, the dissymmetry factor g per definition is an intensive quantity not depending on dimensional parameters such as layer thickness. The original definition is valid for dissolved molecules or small colloidal aggregates not accounting for scatter or reflection which is inherent to the nature of thin films. Actually it is commonly found, that g depends on layer thickness for molecular or polymeric thin films.[39,41–43, 45] A suitable correction for reflection losses can overcome this issue,[28] but this holds true only for smooth and continuous thin layers. For very thick layers like several hundreds of nanometers a cholesteric ordering and Bragg reflection could be found as explanation.[42,43] For thinner but macroscopically ordered samples liquid crystalline blue phases have been proposed to cause the thickness dependent g.[45] For the annealed **nOCi-SQ** samples we can say that the thickness or better roughness dependent g is not an intrinsic material property but an effect caused by the rotationally random micro-morphology of the samples convoluted with the macroscopic probe beam.[52] The impact of such intermediate supra-chiral coupling of likewise chiral supra-molecular aggregates on the chiroptical response of thin film samples is largely underexplored – despite the emerging interest in chiral organic opto-electronics – and deserves further quantitative assessment in the future.

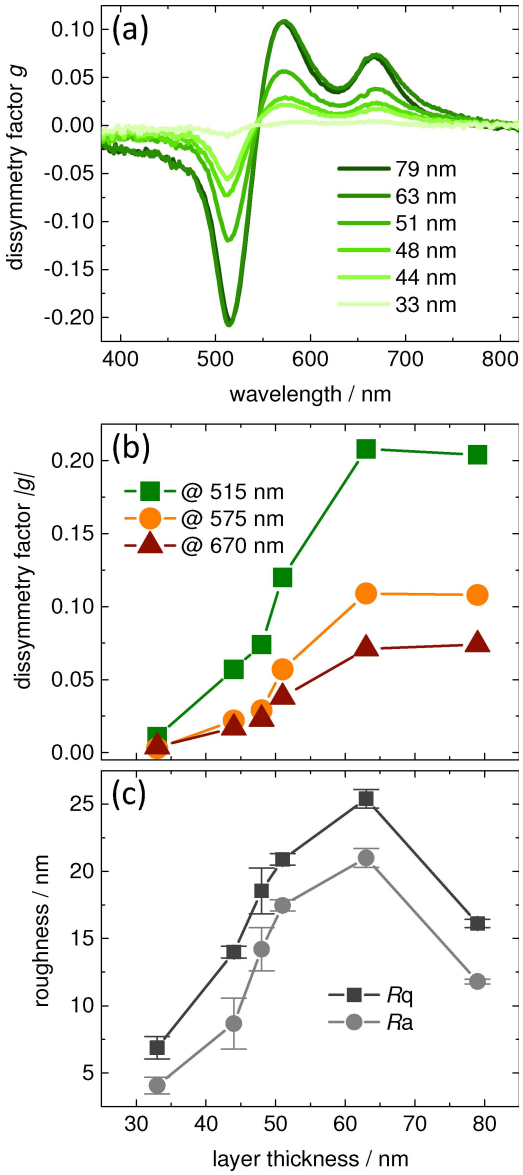

Figure 9. (a) Calculated dissymmetry factor g of spincasted and subsequently at 100 °C annealed **nOCi-SQ** samples with varying coverage. Note that the layer thickness values as indicated in the graph are only nominal estimates as obtained from the ellipsometric fitting procedure due to the micro-morphology of the samples. (b) Dissymmetry factor g peak values versus nominal film thickness for the minimum at 515 nm (squares) and the maximum (circles) at 575 nm of the bisignate CD signal, and for the second peak maximum at 670 nm (triangles). (c) Corresponding average surface roughness Ra and root mean square surface roughness Rq taken from 5 μm×5 μm AFM scans versus nominal layer thickness of the temperature treated **nOCi-SQ** samples.

4. Summary and Conclusion

We have prepared squaraine compounds with indolenine and anilino backbone motifs functionalized with chiral (*S*)-citronellyl groups at the terminal *N* position. Only in case of

the anilino SQ we could obtain chiral aggregation in spincasted and subsequently thermally annealed samples. Their chiroptical response was clearly impacted by morphology: condensation of **nOCi-SQ** into micro-fibrils with random distribution caused the dissymmetry factor g to depend on material coverage. The shape of the **nOCi-SQ** CD spectra is characteristic and independent of micro-texture. It reinforces the interpretation of the double hump spectral signatures previously found for *n*-alkyl anilino SQs to consist of a Coulomb-ICT-hybrid exciton. The exploration of both aspects, impact of charge transfer excitons and micro-morphology on the chiroptical response of organic thin film samples, is still at its infancy. And that is despite the emerge of chiral organic opto-electronics for next-generation devices. We hope to stimulate further basic research in this direction after having introduced a suitable model system.

5. Experimental

5.1 Synthesis

All chemicals were purchased from standard suppliers and used without further purification, all syntheses were done in standard glassware. NMR: ^{1}H and ^{13}C NMR spectra were recorded at 299 K at 500 MHz and 125 MHz. ^{1}H NMR chemical shifts are reported on the δ scale (ppm) relative to the residual non-deuterated solvent as the internal standard. ^{13}C NMR chemical shifts are given in δ values (ppm) relative to the deuterated solvent as the internal standard. Mass spectrometry: ESI mass spectra were taken on Thermo Fisher Scientific Orbitrap XL and Bruker Daltonik micrOTOF–Q spectrometers. UV-vis: UV-vis absorbance spectra were recorded on Analytik Jena Specord 200 using 1 cm Hellma quartz cuvettes. Elemental Analysis: elemental analysis was conducted on Heraeus Vario EL.

(*S*)-3,7-Dimethyloctan-1-ol ((*3S*)-dihydrocitronellol) (8)[53] Under argon atmosphere, 4.3 g (27.5 mmol, 1 eq.) (*S*)-citronellol (7) were dissolved in 30 mL ethyl acetate in a 100 mL Schlenk flask and the mixture was degassed by three freeze-pump-thaw cycles. 430 mg palladium 10% on carbon (1.5 mol%) were added and the mixture was again degassed three times. The argon atmosphere was replaced by a hydrogen atmosphere and the mixture was stirred vigorously. After 16 hours, the mixture was filtrated through Celite® and the residue was extracted with ethyl acetate. The filtrates were combined and the solvent was removed under reduced pressure to obtain the product as a colorless liquid, which was used without further purification (3.54 g, yield: 81%). ORD: $[\alpha]_D^{20} = -3.4°$ ($c = 2$ in $CHCl_3$). The other analytical data are in accordance with the literature.[53]

(*S*)-3,7-Dimethyloctyl-*p*–toluenesulfonate (9)[33] Under argon atmosphere, 1.5 g (9.5 mmol, 1 eq.) (*S*)-3,7-dimethyl-1-octanol (**8**) were suspended in 5 mL pyridine abs. and cooled to 10 °C. To the reaction mixture, 3.62 g (19.0 mmol, 2 eq.) tosyl chloride were added in portions under stirring over 30 minutes. After warming to room temperature and stirring for additional 24 hours, the mixture was poured into ice-cold 3 N hydrochloric acid and extracted with diethyl ether. The combined organic phases were washed with water and brine and dried over sodium sulphate. After removal of the solvents under reduced pressure, the raw product was obtained as a yellow oil and purified by column chromatography (silica gel) with dichloromethane/cyclohexane (1 : 1, v/v) as the eluent. The purified product was obtained as a colourless oil (1.24 g, yield: 41%). ORD: $[\alpha]_D^{20} = -2.6°$ ($c = 1$ in $CHCl_3$). The other analytical data are in accordance with the reported values of the racemic mixture.[33]

(*S*)-1-(3,7-Dimethyloctyl)-2,3,3-trimethyl-3*H*-indole-1-iumtosylate (10)[34] Under argon atmosphere, 478 mg (3 mmol, 1 eq.) 2,3,3-trimethyl-3*H*-indole (**1**) and 937 mg (3 mmol, 1 eq.) (*S*)-3,7-dimethyloctyl-p-toluenesulfonate (**9**) were dissolved in 5 mL nitromethane abs. and refluxed for 16 hours. The mixture was cooled to room temperature and the solvents were partially removed under reduced pressure. The residue was mixed with diethyl ether and the precipitate was collected, washed with diethyl ether, and dried under vacuum. The product was obtained as a wine-red solid. (1.10 g, yield: 78%) The analytical data are in accordance with the reported values of the racemic mixture.[34]

(*S,S*)-1,3-Bis[(1-(3,7-dimethyloctyl)-2,3-dihydro-3,3-dimethyl-1H-indol-2-yl)methyl]-squaraine ((*S,S*)-bCi-SQ)[35] In a flask with affixed Dean-Stark apparatus and reflux condenser 500 mg (1.06 mmol, 2 eq.) (*S*)-1-(3,7-dimethyloctyl)-2,3,3-trimethyl-3*H*-indol-1-iumtosylate (10) and 60 mg (0.53 mmol, 1 eq.) squaric acid (3) were suspended in a mixture of 5 mL butanol, 5 mL toluene and 2 mL pyridine. The mixture was refluxed under argon atmosphere for 18 hours. After removal of the solvents under reduced pressure the raw product was purified by column chromatography (silica gel) with cyclohexane/ethyl acetate (gradient elution, 3 : 1 to 2 : 1, v/v) as the eluent. The product was dissolved in small amounts of dichloromethane, diluted in an excess of *n*-hexane, and stored at 2 °C. The precipitate was collected and washed with cold *n*-hexane. The purified product was obtained as green-golden crystals (184 mg, yield: 51%). ^{1}H NMR: (500 MHz, chloroform-*d*) δ [ppm] = 7.35 (dd, ^{3}J = 7.4 Hz, ^{4}J = 1.2 Hz, 2H), 7.30 (ddd, ^{3}J = 7.7 Hz, ^{4}J = 1.2 Hz, 2H), 7.14 (ddd, ^{3}J = 7.5 Hz, ^{4}J = 0.9 Hz, 2H), 6.96 (d, ^{3}J = 7.9 Hz, 2H), 5.98 (s, 2H), 4.08–3.93 (m, 4H), 1.79 (s, 14H), 1.65–1.58 (m, 4H), 1.56–1.48 (m, 2H), 1.43–1.29 (m, 4H), 1.30–1.18 (m, 4H), 1.18–1.11 (m, 4H), 1.04 (d, ^{3}J = 6.0 Hz, 6H), 0.86 (d, ^{3}J = 6.6 Hz, 12H). ^{13}C NMR: (126 MHz, chloroform-*d*) δ [ppm] = 182.4, 170.1, 142.5, 127.9, 123.8, 122.4, 109.4, 86.7, 49.4, 42.3, 39.3, 37.3, 34.0, 31.3, 28.1, 27.2, 24.8, 22.8, 22.7, 19.7. MS (ESI+): m/z = 677.5 $[M+H]^+$. MS (ESI HRMS): m/z calcd for $C_{46}H_{64}N_2O_2H$ $[M+H]^+$: 677.5041, found: 677.5047. m/z calcd for $C_{46}H_{64}N_2O_2$ $M^{\bullet+}$: 676.4962, found: 676.4969. UV/vis: (toluene) λ_{max} = 644 nm. Elemental Analysis: calcd for $C_{46}H_{64}N_2O_2 \cdot 0.1\ CH_2Cl_2 \cdot 0.5\ C_6H_{14}$: C: 80.94; H: 9.85; N: 3.84, found: C: 80.95; H: 9.87; N: 3.53.

(*S*)-[(1-(3,7-dimethyloctyl)-2,3-dihydro-3,3-dimethyl-1*H*-indol-2-yl)methyl]-squaraine ((*S*)-mCi-SQ) In a flask with affixed Dean-Stark apparatus and reflux condenser 250 mg (0.51 mmol, 1 eq.) (*S*)-1-(3,7-dimethyloctyl)-2,3,3-trimethyl-3H-indol-1-iumtosylate (**10**) and 150 mg (0.53 mmol, 1 eq.) 3-((1-ethyl-3,3-dimethylindolin-2-ylidene) methyl)-4-hydroxycyclobut-3-ene-1,2-dione (**6**) were suspended in a mixture of 5 mL butanol, 5 mL toluene and 2 mL pyridine. The mixture was refluxed under argon atmosphere for 18 hours. After removal of the solvents under reduced pressure the raw product was purified by column chromatography (silica gel) with cyclohexane/acetone (2 : 1, v/v) as the eluent. The product was dissolved in small amounts of dichloromethane, diluted in an excess of *n*-hexane, and stored at 2 °C. The precipitate was collected and washed with cold *n*-hexane. The purified product was obtained as a green powder (134 mg, yield: 41 %). ^{1}H NMR: (500 MHz, acetone-d_6) δ [ppm] = 7.54–7.46 (m, 2H), 7.42–7.34 (m, 2H), 7.28 (d, ^3J = 7.9 Hz, 1H), 7.24 (d, ^3J = 7.9 Hz, 1H), 7.22–7.15 (m, 2H), 5.96 (s, 1H), 5.94 (s, 1H), 4.21 (d, ^3J = 7.2 Hz, 2H), 4.25–4.13 (m, 2H), 1.89–1.80 (m, 1H), 1.77 (s, 12H, H-6), 1.73–1.66 (m, 1H), 1.66–1.59 (m, 1H), 1.59–1.49 (m, 1H), 1.49–1.42 (m, 1H), 1.39 (t, ^3J = 7.2 Hz, 3H), 1.42–1.22 (m, 3H, H-30b), 1.22–1.16 (m, 2H), 1.08 (d, ^3J = 6.4 Hz, 3H), 0.86 (2x d, ^3J = 6.6 Hz, 6H). ^{13}C NMR: (126 MHz, acetone-d_6) δ [ppm] = 182.3, 182.1, 181.8, 170.1, 169.9, 143.4, 143.1, 142.9, 142.9, 128.8, 128.8, 124.5, 124.4, 123.1, 110.6, 110.5, 87.3, 87.0, 49.9, 49.9, 42.5, 39.9, 38.9, 37.8, 34.4, 28.7, 27.4, 27.3, 27.3, 25.5, 23.0, 22.9, 20.1, 12.2. MS (ESI+): m/z = 564.4 $M^{\bullet+}$, 1129.8 $[2M+H]^+$. MS (ESI HRMS): m/z calcd for $C_{38}H_{48}N_2O_2$ $M^{\bullet+}$: 564.3710, found: 564.3705. UV/vis: (toluene) λ_{max} = 642 nm. Elemental Analysis: calcd for $C_{38}H_{48}N_2O_2 \cdot 0.05\ CH_2Cl_2 \cdot 0.05\ C_6H_{14}$: C: 80.34; H: 8.58; N: 4.89, found: C: 80.16; H: 8.47; N: 4.75.

***N*-(*S*)-(3,7-Dimethyl-6-octenyl)-*N*-octylamine (11)** (*S*)-(-)-3,7-Dimethyl-6-octenal (7.01 g, 45.38 mmol) and octylamine (6.07 g, 47.00 mmol) are dissolved in 30 ml of MeOH. The colorless solution is stirred at r.t. overnight. $NaBH_4$ (3.00 g, 79.30 mmol) is added portion wise to the solution and the mixture is stirred at r.t. for 30 min. The solution is then poured in 400 ml of 1 M NaOH and the resulting mixture is extracted with Et_2O (3 × 150 ml). Combined organic phase was washed with water (2 × 200 ml), dried over powdered KOH and evaporated to dryness to give alight yellow oil (10.5 g, 39.25 mmol, yield 87 %). ^{1}H NMR ($CDCl_3$) δ 5.05 (m, 1H), 3.14 (t, J = 7.5 Hz, 2H), 3.12 (t, J = 7.5 Hz, 2H), 2.84 (s, 3H), 1.96 (m, 2H), 1.65 (s, 3H), 1.61 (s, 3H), 1.70-1.09 (m, 17H), 0.90 (d, J = 6.6 Hz, 3H), 0.87 (t, J = 7.2 Hz, 3H).

1,3-bis[4-(*N*-(*S*)-3,7-Dimethyl-6-octenyl)-*N*-octylamine)-2,6-dihydroxyphenyl]-squaraine ((*S,S*)-nOCi-SQ) *N*-(*S*)-(3,7-Dimethyl-6-octenyl)-*N*-octylamine (6.00 g, 22.43 mmol) and phloroglucinol (1.50 g, 11.90 mmol) are suspended in a 1 : 4 vol mixture of nBuOH:toluene (50 ml). Mixture is refluxed under a Dean-Stark trap until no more water is collected (about 1 h). Volatiles are removed and the solid residue is taken up with a 1 : 1 vol mixture of nBuOH:toluene (50 ml). Squaric acid (0.68 g, 5.95 mmol) is added, and mixture refluxed under a Dean-Stark trap for 2 h. All volatiles are removed, and the dark oily residue is taken up with MeOH (60 ml) to give a golden green precipitated that is collected by filtration and crystallized from EtOH to give the pure title compound as a dark green solid with a metallic luster (1.02 g, 1.23 mmol, 20.7 % yield). ^{1}H NMR (CD_2Cl_2) δ 10.88 (s, 4H), 5.80 (s, 4H), 5.15 (t, J = 7.2 Hz, 2H), 3.45-3.35 (m, 8H), 2.10-1.95 (m, 4H), 1.73 (s, 6H), 1.66 (s, 12H), 1.56-1.48 (m, 4H), 1.40-1.30 (m, 24H), 1.00 (d, J = 6.0 Hz, 6H), 0.93 (t, J = 6.0 Hz, 6H); ^{13}C NMR (CD_2Cl_2) δ 181.3, 162.6, 160.5, 157.8, 131.4, 124.4, 102.1, 93.4, 51.5, 49.8, 36.9, 34.6, 31.8, 30.7, 29.3, 29.2, 28.0, 27.0 25.4, 25.3, 22.6, 19.2, 17.4, 13.9. Anal Calcd For $C_{52}H_{80}N_2O_6$: C, 75.32; H, 9.72; N, 3.38. Found: C, 75.08; H, 9.83; N, 3.29.

5.2 Single Crystal Structure Analysis

Single crystals of **(*S,S*)-bCi-SQ** suitable for X-ray diffraction analysis were directly obtained from the purification procedure. A selected crystal was measured with a Bruker AXS Kappa Apex II CCD diffractometer at 100 K using graphite-monochromated Mo-Kα radiation (λ = 0.71073 Å).

Crystal dimensions 0.300 mm × 0.200 mm × 0.150 mm, metallic-green-blue block, empirical formula $C_{52}H_{78}N_2O_2$ and weight 763.16 amu, monoclinic, space group I2, a = 19.0769(7) Å, b = 9.3541(4) Å, c = 27.3099(13) Å, $\alpha = \gamma = 90°$, β = 108.953(2)°, V = 4609.2(3) Å^3, Z = 4, density 1.100 g/cm^3, absorption coefficient 0.065 mm^{-1}, F(000) = 1680, theta range for data collection 1.753° to 30.032°, index ranges $-26 \le h \le 26, -13 \le k \le 13, -38 \le l \le 38$, 173568 reflections collected (13500 unique, $R_{(int)}$ = 0.0390, observed reflections ($I > 2(I)$) 12474, completeness to theta = 30.032° 100 %, semi-empirical from equivalents absorption correction, max and min transmission 1.0000 and 0.9624, final R indices ($I > 2\sigma(I)$) $R1 = 0.0410$, $wR2 = 0.1055$, R induces (all data) $R1 = 0.0464$, $wR2 = 0.1093$, full-matrix least-squares on F^2 refinement, GOF on F^2 = 1.083 for 13500 data and 1 restraint and 526 parameters, largest diff. peak and hole 0.396 eÅ^{-3} and −0.240 eÅ^{-3}.

The structures were solved with SHELXS-2013/1 and then refined with the SHELXL 2018/3.[54] The crystallographic data file can be found online at the Cambridge Crystallographic Data Centre under the CCDC code 2094899. The single crystal structure data were analyzed with VESTA 3.5.7[55] and are visualized with Mercury 4.2.0.[56]

5.3 Thin Film Sample Preparation

The molecular compounds were dissolved on amylene-stabilized chloroform at concentrations of 4 mg/mL, 5 mg/mL, or 6 mg/mL and spincoated onto float glass substrates (15 mm × 15 mm) cut from float glass objectives slides (VWR) at variable rotation speeds to obtain layers of varying thick-

ness. Optional subsequent thermal annealing typically for 30 minutes on a preheated hot plate (temperatures as indicated in the text) was applied to induce controlled aggregation of the molecular compounds. Preparation was either conducted in inert nitrogen atmosphere or under ambient conditions, which had no effect on the sample quality.

5.4 Spatially Resolved Optical and Morphological Characterization

The morphology of the thin film samples was obtained by atomic force microscopy (AFM, JPK NanoWizard) in intermittent contact mode. Tap300-G cantilevers from Budget-Sensors were used for imaging. AFM images were analyzed either by Gwyddion 2.59[57] or by the JPK SPM data processing software, version 5.0.133.

The optical micro-structure of the samples was characterized using a Leica DMRME polarization microscope. Both, images in reflection with a single or two crossed polarizers as well as images in transmission were taken. The microscope was coupled to a miniature spectrometer (Ocean Optics Maya2000) through a 200 µm optical fiber, allowing to take local transmission spectra from a spot size of about 30 µm diameter. A simple polarization analysis was obtained by adding a linear polarizer behind the sample and rotating the sample by a computer controlled rotation stage (Thorlabs PRM1Z8).

5.5 Ellipsometry and Mueller Matrix Polarimetry

Standard spectroscopic ellipsometric scans to obtain Ψ and Δ in reflection (45°–75° in steps of 5°) have been obtained with a J.A. Woollam M-2000 DI or XI rotating compensator instrument with horizontal sample stage. The spectral range from 193 nm or 245 nm to 1690 nm containing 690 or 660 wavelengths is recorded with a CCD-array detector. For unpolarized normal incidence transmission intensity spectra a custom-made sample holder was used. The complex refractive index was fitted using the vendor provided software CompleteEASE version 6. The multiple sample analysis feature was used for combined fitting of samples with variable layer thickness and to include transmission intensity data (1000 % fit weighting).[58] Incoherent backside reflections from the glass substrate and depolarization data have been included in the fit routine. The Kramers Kronig consistent B-spline with spectral node spacing of 0.1 eV was used to obtain a best match of fitted and experimental data. Optionally, anisotropic fitting (type uniaxial, difference mode off) was applied to obtain two sets of the complex refractive index: ordinary (in-plane) within the thin film plane, and extra-ordinary (out-of-plane) perpendicular to the extended thin film.[14] Note that the collimated beam diameter of approximately 3 mm does not provide spatial resolution but returns effective or averaged dielectric properties of textured thin films.

To extract the circular dichroism from the thin films, Mueller matrix recording in normal incidence transmission were performed with the J.A. Woollam DI or XI using a custom-made sample holder. Due to the polarizer-compensator-sample-analyzer (PCSA) configuration of the instruments, only the first three rows (12 elements out of 16) of the normalized Mueller matrix could be obtained. The complete normalized Mueller matrix **M** (all 16 elements with $m11 = 1$) is recovered by an algebraic procedure, which is applicable due to reasonably low depolarization effects.[59] The differential, recovered non-depolarizing Mueller matrix **L** provides the following physical interpretation of the matrix elements in case of normal incidence transmission recording:[28,60]

$$\mathbf{L} = \ln(\mathbf{M}) = \begin{pmatrix} 0 & -\mathrm{LD} & -\mathrm{LD}' & \mathrm{CD} \\ -\mathrm{LD} & 0 & \mathrm{CB} & \mathrm{LB}' \\ -\mathrm{LD}' & -\mathrm{CB} & 0 & -\mathrm{LB} \\ \mathrm{CD} & -\mathrm{LB}' & \mathrm{LB} & 0 \end{pmatrix} \quad (1)$$

with CD: circular dichroism, CB: circular birefringence, LD: horizontal linear dichroism, LB: horizontal linear birefringence, LD': 45° linear dichroism, LB': 45° linear birefringence.

Differential, recovered Mueller matrix data for selected **nOCi-SQ** samples can be seen in the Supporting Information in Figure S4.

The circular dichroism value CD is then taken as the average of the $l14$ and $l41$ elements. Note that CD is not the same as the ellipticity θ as typical output of a conventional CD-spectrometer:

$$\theta = \arctan\left(\frac{e^{\mathrm{CD}} - 1}{e^{\mathrm{CD}} + 1}\right) \quad (2)$$

Only for small CD quantities the following approximation $\theta = \mathrm{CD}/2$ holds true. An obvious benefit of the Mueller matrix polarimetry approach to circular dichroism studies is, that the provided CD value is free from linear dichroism contribution. This makes the approach most suitable for the analysis of thin film samples.

The dissymmetry factor g[23–25] is defined as the circular dichroism in "units of absorbance" $\Delta Abs^{\mathrm{CP}} = Abs^{\mathrm{LCP}} - Abs^{\mathrm{RCP}} = \frac{2}{\ln(10)} \cdot \mathrm{CD}$ normalized to the unpolarized absorbance $Abs = -\log(T)$ calculated from the transmission T:

$$g = \frac{\Delta Abs^{\mathrm{CP}}}{Abs} \quad (3)$$

This definition applies for spectroscopy of samples in solution, where the absorbance basically does not include contributions from reflection, scatter and thin film interference. Therefore, a true dissymmetry factor is supposed to be

an intensive quantity, a unique measure for the material property, not depending on dimensional aspects of the sample. For thin film samples, the dissymmetry factor requires cumbersome refinement accounting for inherent reflection, interference, scatter, and in case of discontinuous micro-structured samples–as in case of spincasted and thermally annealed **nOCi-SQ** also other morphology related aspects. Especially the latter would require spatially resolved CD analysis, and therefore, is beyond the scope of the present study. Thus, we adhere to the original definition of the dissymmetry factor *g*.

Acknowledgements

MS*, MS and JZ are obliged to the DFG for funding within GRK 1885 "Molecular Basis of Sensory Biology". MS* thanks the PRO RETINA Stiftung for personal funding. MS*, NSS and MFS acknowledge the Linz Institute of Technology (LIT-2019-7-INC-313 SEAMBIOF) for funding. MFS, AL and KM are obliged to the DFG GRK 2591 "Template-designed Organic Electronics – TIDE" for financial support. MS* is grateful to Prof. Kurt Hingerl and the ZONA team for inspiration and support as well as Dr. Munise Cobet from the LIOS team.

References

[1] S. Sreejith, P. Carol, P. Chithra, A. Ajayaghosh, *J. Mater. Chem.* **2008**, *18*, 264–274.
[2] L. Beverina, M. Sassi, *Synlett* **2014**, *25*, 477–490.
[3] G. Xia, H. Wang, *J. Photochem. Photobiol. C* **2017**, *31*, 84–113.
[4] K. Ilina, W. M. MacCuaig, M. Laramie, J. N. Jeouty, L. R. McNally, M. Henary, *Bioconjugate Chem.* **2019**, *31*, 194–213.
[5] C. Qin, W. Y. Wong, L. Han, *Chem. Asian J.* **2013**, *8*, 1706–1719.
[6] G. Chen, H. Sasabe, T. Igarashi, Z. Hong, J. Kido, *J. Mater. Chem. A* **2015**, *3*, 14517–14534.
[7] M. Jo, S. Choi, J. H. Jo, S. Y. Kim, P. S. Kim, C. H. Kim, H. J. Son, C. Pac, S. O. Kang, *ACS Omega* **2019**, *4*, 14272–14283.
[8] Y. Chen, W. Zhu, J. Wu, Y. Huang, A. Facchetti, T. J. Marks, *Org. Photonics Photovolt.* **2019**, *6*, 1–16.
[9] J. He, Y. J. Jo, X. Sun, W. Qiao, J. Ok, T. il Kim, Z. Li, *Adv. Funct. Mater.* **2020**, *31*, 2008201.
[10] E. Lima, O. Ferreira, J. F. Silva, A. O. Santos, R. E. Boto, J. R. Fernandes, P. Almeida, S. M. Silvestre, L. V. Reis, *Dyes Pigm.* **2020**, *174*, 108024.
[11] K. Strassel, W. H. Hu, S. Osbild, D. Padula, D. Rentsch, S. Yakunin, Y. Shynkarenko, M. Kovalenko, F. Nüesch, R. Hany, M. Bauer, *Sci. Technol. Adv. Mater.* **2021**, *22*, 194–204.
[12] N. J. Hestand, F. C. Spano, *Chem. Rev.* **2018**, *118*, 7069–7163.
[13] F. Balzer, H. Kollmann, M. Schulz, G. Schnakenburg, A. Lützen, M. Schmidtmann, C. Lienau, M. Silies, M. Schiek, *Cryst. Growth Des.* **2017**, *17*, 6455–6466.
[14] J. Zablocki, M. Schulz, G. Schnakenburg, L. Beverina, P. Warzanowski, A. Revelli, M. Grüninger, F. Balzer, K. Meerholz, A. Lützen, M. Schiek, *J. Phys. Chem. C* **2020**, *124*, 22721–22732.
[15] C. Zhong, D. Bialas, C. J. Collison, F. C. Spano, *J. Phys. Chem. C* **2019**, *123*, 18734–18745.
[16] U. Mayerhöffer, M. Gsänger, M. Stolte, B. Fimmel, F. Würthner, *Chem. Eur. J.* **2012**, *19*, 218–232.
[17] U. Mayerhöffer, K. Deing, K. Gruß, H. Braunschweig, K. Meerholz, F. Würthner, *Angew. Chem. Int. Ed.* **2009**, *48*, 8776–8779; *Angew. Chem.* **2009**, *121*, 8934–8937.
[18] G. M. Paternò, N. Barbero, S. Galliano, C. Barolo, G. Lanzani, F. Scotognella, R. Borrelli, *J. Mater. Chem. C* **2018**, *6*, 2778–2785.
[19] C. A. Shen, D. Bialas, M. Hecht, V. Stepanenko, K. Sugiyasu, F. Würthner, *Angew. Chem. Int. Ed.* **2021**, *60*, 11949–11958.
[20] J. H. Kim, A. Liess, M. Stolte, A. M. Krause, V. Stepanenko, C. Zhong, D. Bialas, F. Spano, F. Würthner, *Adv. Mater.* **2021**, *33*, 2100582.
[21] T. Maeda, A. Liess, A. Kudzus, A. M. Krause, M. Stolte, H. Amitani, S. Yagi, H. Fujiwara, F. Würthner, *Chem. Commun.* **2020**, *56*, 9890–9893.
[22] C. Zheng, D. Bleier, I. Jalan, S. Pristash, A. R. Penmetcha, N. J. Hestand, F. C. Spano, M. S. Pierce, J. A. Cody, C. J. Collison, *Sol. Energy Mater. Sol. Cells* **2016**, *157*, 366–376.
[23] G. Pescitelli, L. D. Bari, N. Berova, *Chem. Soc. Rev.* **2011**, *40*, 4603.
[24] M. Liu, L. Zhang, T. Wang, *Chem. Rev.* **2015**, *115*, 7304–7397.
[25] G. Albano, G. Pescitelli, L. D. Bari, *Chem. Rev.* **2020**, 120, 10145–10243.
[26] J. Selby, M. Holzapfel, B. K. Lombe, D. Schmidt, A. M. Krause, F. Würthner, G. Bringmann, C. Lambert, *J. Org. Chem.* **2020**, *85*, 12227–12242.
[27] J. Zablocki, O. Arteaga, F. Balzer, D. Hertel, J. J. Holstein, G. Clever, J. Anhäuser, R. Puttreddy, K. Rissanen, K. Meerholz, A. Lützen, M. Schiek, *Chirality* **2020**, *32*, 619–631.
[28] M. Schulz, J. Zablocki, O. S. Abdullaeva, S. Brück, F. Balzer, A. Lützen, O. Arteaga, M. Schiek, *Nat. Commun.* **2018**, *9*, 2413.
[29] A. Painelli, University di Parma, Italy, private communication.
[30] M. Schulz, F. Balzer, D. Scheunemann, O. Arteaga, A. Lützen, S. C. J. Meskers, M. Schiek, *Adv. Funct. Mater.* **2019**, *29*, 1900684.
[31] J. R. Brandt, F. Salerno, M. J. Fuchter, *Nat. Chem. Rev.* **2017**, 1, 0045.
[32] J. L. Greenfield, J. Wade, J. R. Brandt, X. Shi, T. J. Penfold, M. J. Fuchter, *Chem. Sci.* **2021**, *12*, 8589–8602.
[33] C. V. Yelamaggad, U. S. Hiremath, S. A. Nagamani, D. S. Rao, S. K. Prasad, N. Iyi, T. Fujita, *Liq. Cryst.* **2003**, *30*, 681–690.
[34] S. F. Voelker, C. Lambert, *Chem. Mater.* **2012**, *24*, 2541–2553.
[35] S. F. Völker, T. Dellermann, H. Ceymann, M. Holzapfel, C. Lambert, *J. Polym. Sci. Part A* **2014**, *52*, 890–911.
[36] H. Ceymann, M. Balkenhohl, A. Schmiedel, M. Holzapfel, C. Lambert, *Phys. Chem. Chem. Phys.* **2016**, 18, 2646–2657.
[37] W. Jin, T. Fukushima, M. Niki, A. Kosaka, N. Ishii, T. Aida, *Proc. Nat. Acad. Sci.* **2005**, *102*, 10801–10806.
[38] T. Seki, A. Asano, S. Seki, Y. Kikkawa, H. Murayama, T. Karatsu, A. Kitamura, S. Yagai, *Chem. Eur. J.* **2011**, *17*, 3598–3608.
[39] G. Lakhwani, G. Koeckelberghs, S. Meskers, R. Janssen, *Chem. Phys. Lett.* **2007**, *437*, 193–197.
[40] J. Gilot, R. Abbel, G. Lakhwani, E. W. Meijer, A. P. H. J. Schenning, S. C. J. Meskers, *Adv. Mater.* **2010**, *22*, E131–E134.
[41] R. Abbel, A. P. H. J. Schenning, E. Meijer, *J. Polym. Sci. Part A* **2009**, *47*, 4215–4233.
[42] G. Lakhwani, S. C. J. Meskers, *J. Phys. Chem. A* **2011**, *116*, 1121–1128.
[43] C. Kulkarni, D. D. Nuzzo, E. Meijer, S. C. Meskers, *J. Phys. Chem. B* **2017**, *121*, 11520–11527.

[44] T. Yamada, K. Nomura, M. Fujiki, *Macromolecules* **2018**, *51*, 2377–2387.
[45] J. Wade, J. N. Hilfiker, J. R. Brandt, L. Liirò-Peluso, L. Wan, X. Shi, F. Salerno, S. T. J. Ryan, S. Schöche, O. Arteaga, T. Jávorfi, G. Siligardi, C. Wang, D. B. Amabilino, P. H. Beton, A. J. Campbell, M. J. Fuchter, *Nat. Commun.* **2020**, *11*, 6137.
[46] J. H. Yum, P. Walter, S. Huber, D. Rentsch, T. Geiger, F. Nüesch, F. D. Angelis, M. Grätzel, M. K. Nazeeruddin, *J. Am. Chem. Soc.* **2007**, *129*, 10320–10321.
[47] C. H. Chang, Y. C. Chen, C. Y. Hsu, H. H. Chou, J. T. Lin, *Org. Lett.* **2012**, *14*, 4726–4729.
[48] M. S. Vezie, S. Few, I. Meager, G. Pieridou, B. Dörling, R. S. Ashraf, A. R. Goñi, H. Bronstein, I. McCulloch, S. C. Hayes, M. Campoy-Quiles, J. Nelson, *Nat. Mater.* **2016**, *15*, 746–753.
[49] S. Funke, M. Duwe, F. Balzer, P. H. Thiesen, K. Hingerl, M. Schiek, *J. Phys. Chem. Lett.* **2021**, *12*, 3053–3058.
[50] J. H. Freudenthal, E. Hollis, B. Kahr, *Chirality* **2009**, *21*(1E), E20–E27.
[51] A. Mendoza-Galván, E. Muñoz-Pineda, S. J. L. Ribeiro, M. V. Santos, K. Järrendahl, H. Arwin, *J. Opt.* **2018**, *20*, 024001.
[52] M. H. Kim, L. Ulibarri, D. Keller, M. F. Maestre, C. Bustamante, *J. Chem. Phys.* **1986**, *84*, 2981–2989.
[53] T. Yamamoto, A. Shimada, T. Ohmoto, H. Matsuda, M. Ogura, T. Kanisawa, *Flavour Fragrance J.* **2004**, *19*, 121–133.
[54] G. M. Sheldrick, *Acta Crystallogr. Sect. C* **2015**, *71*, 3–8.
[55] K. Momma, F. Izumi, *J. Appl. Crystallogr.* **2011**, *44*, 1272–1276.
[56] C. F. Macrae, I. Sovago, S. J. Cottrell, P. T. Galek, P. Mc–Cabe, E. Pidcock, M. Platings, G. P. Shields, J. S. Stevens, M. Towler et al., *J. Appl. Crystallogr.* **2020**, *53*, 226–235.
[57] D. Necas, P. Klapetek, *Cent. Eur. J. Phys.* **2012**, *10*, 181–188.
[58] J. N. Hilfiker, N. Singh, T. Tiwald, D. Convey, S. M. Smith, J. H. Baker, H. G. Tompkins, *Thin Solid Films* **2008**, *516*, 7979–7989.
[59] O. Arteaga, R. Ossikovski, *J. Opt. Soc. Amer. A* **2019**, *36*, 416.
[60] O. Arteaga, B. Kahr, *Opt. Lett.* **2013**, *38*, 1134.

Manuscript received: July 25, 2021
Version of record online: ■■, ■■

RESEARCH ARTICLE